Supporting Information

Redox Trends in Cyclometalated Palladium(II) Complexes

Yulia B. Dudkina[a], Kirill V. Kholin[a], Tatyana V. Gryaznova[a], Daut R. Islamov[a,b], Olga N. Kataeva[a,b], Ildar Kh. Rizvanov,[a] Alina I. Levitskaya[a], Olga D. Fominykh[a], Marina Yu. Balakina[a], Oleg G. Sinyashin[a], Yulia H. Budnikova[a] *

[a] *A.E. Arbuzov Institute of Organic and Physical Chemistry, Kazan Scientific Center, Russian Academy of Sciences, 8 Arbuzov str., Kazan 420088, Russian Federation*

[b] *b. Kazan (Volga Region) Federal University, A.M. Butlerov Chemical Institute, 18 Kremlevskaya str., Kazan, 420008, Russian Federation, 18 Kremlevskaya str., Kazan, 420008, Russian Federation*

Electrochemical details

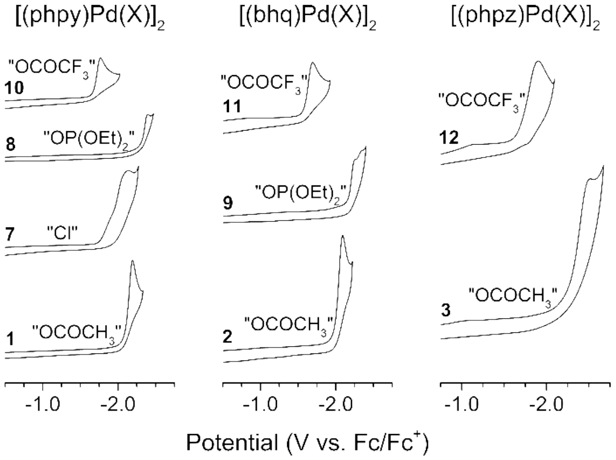

Fig. S1 Cyclic voltammograms of palladacycles reduction in CH_3CN.

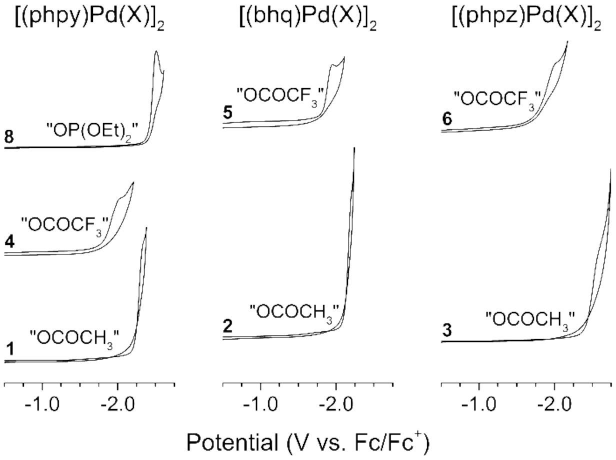

Fig. S2 Cyclic voltammograms of palladacycles reduction in CH_2Cl_2.

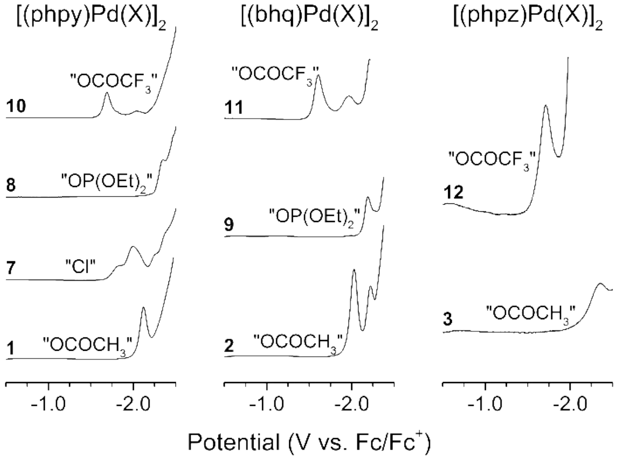

Fig. S3 Differential pulse voltammograms of palladacycles reduction in CH_3CN.

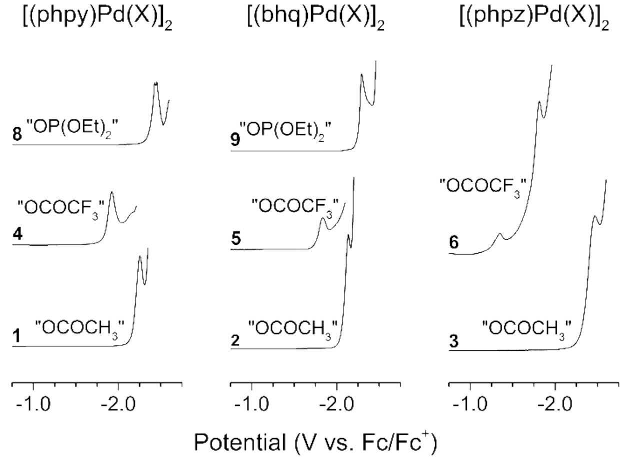

Fig. S4 Differential pulse voltammograms of palladacycles reduction in CH_2Cl_2.

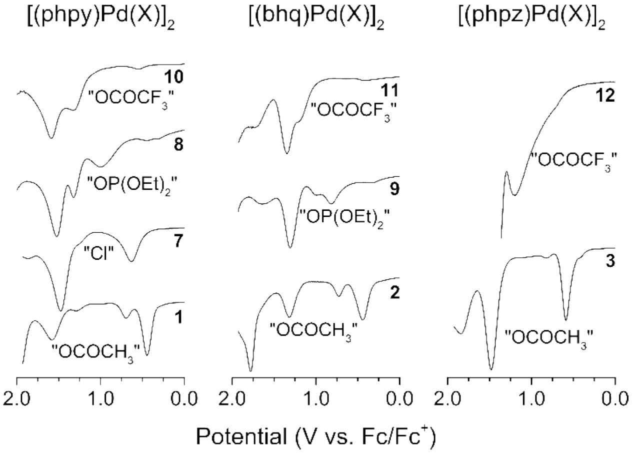

Fig. S5 Differential pulse voltammograms of palladacycles oxidation in CH_3CN.

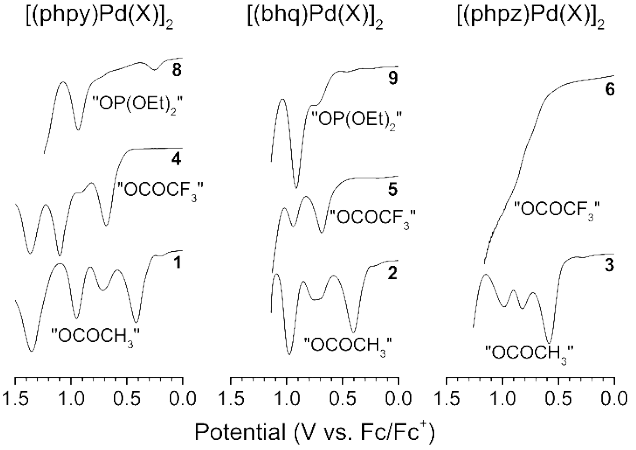

Fig. S6 Differential pulse voltammograms of palladacycles oxidation in CH_2Cl_2.

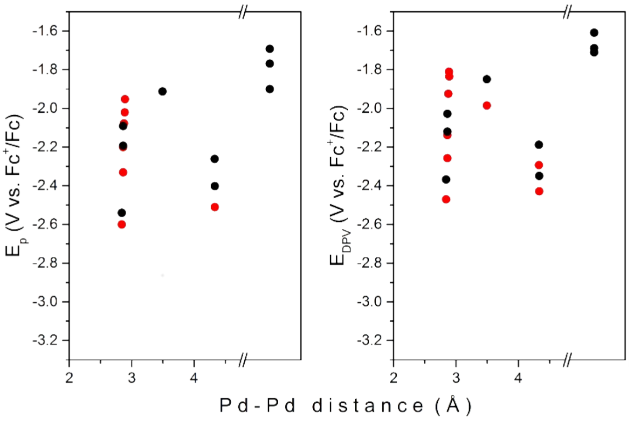

Fig. S7 Plots of reduction potential vs Pd-Pd distance: peak potential (left), potential determined by DPV (right). Red dots – reductions in CH_2Cl_2, black dots – reductions in CH_3CN.

ESR details

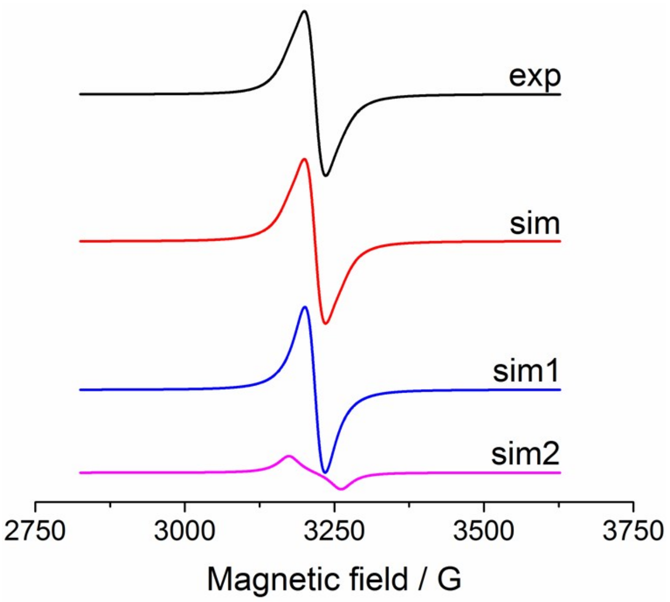

Fig. S8 Characteristic simulation of a Pd(III) ESR spectra: black line – experimental spectrum, red line - a sum of blue (simulation considering only ^{104}Pd atoms) and purple (simulation considering only ^{105}Pd atoms) lines.

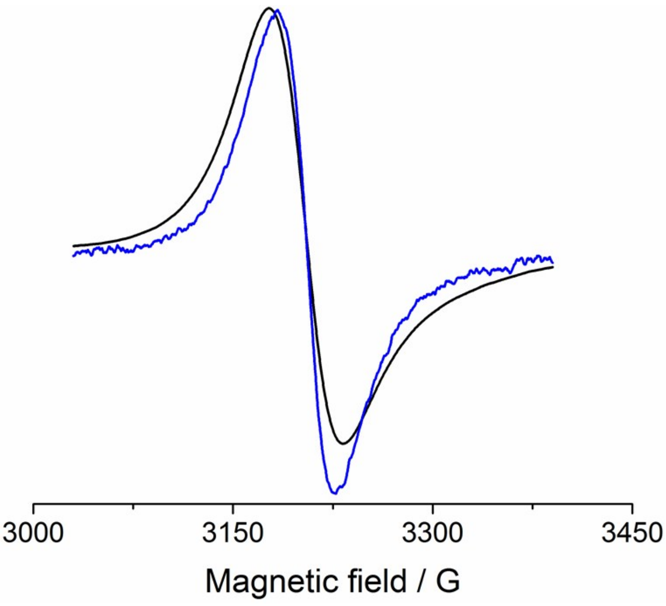

Fig. S9 Normalized ESR spectra of **4** with concentrations 0.005 M (blue) and 0.1 M (black) at 295 K.

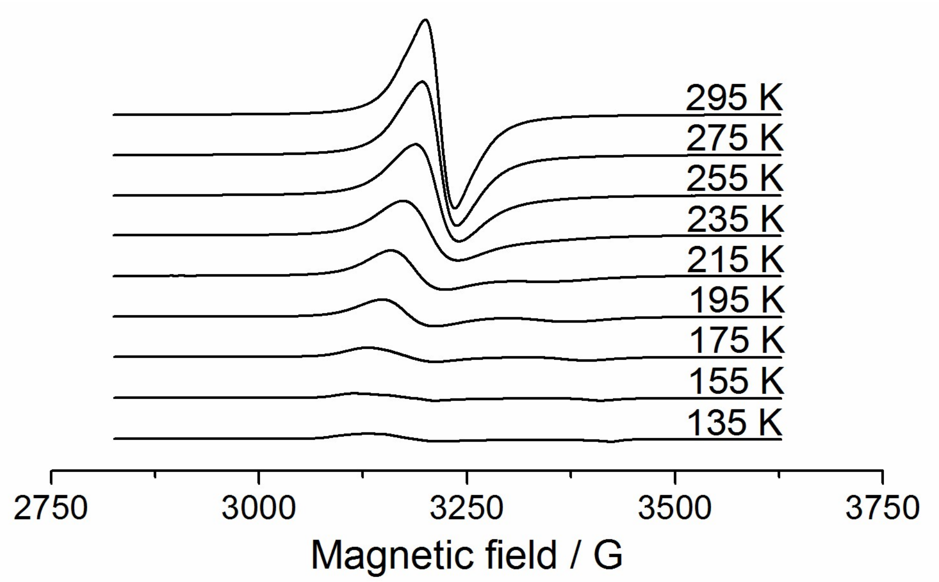

Fig. S10 Temperature dependence of complex **1** ESR spectrum in CH_2Cl_2 upon oxidation (0.1 M).

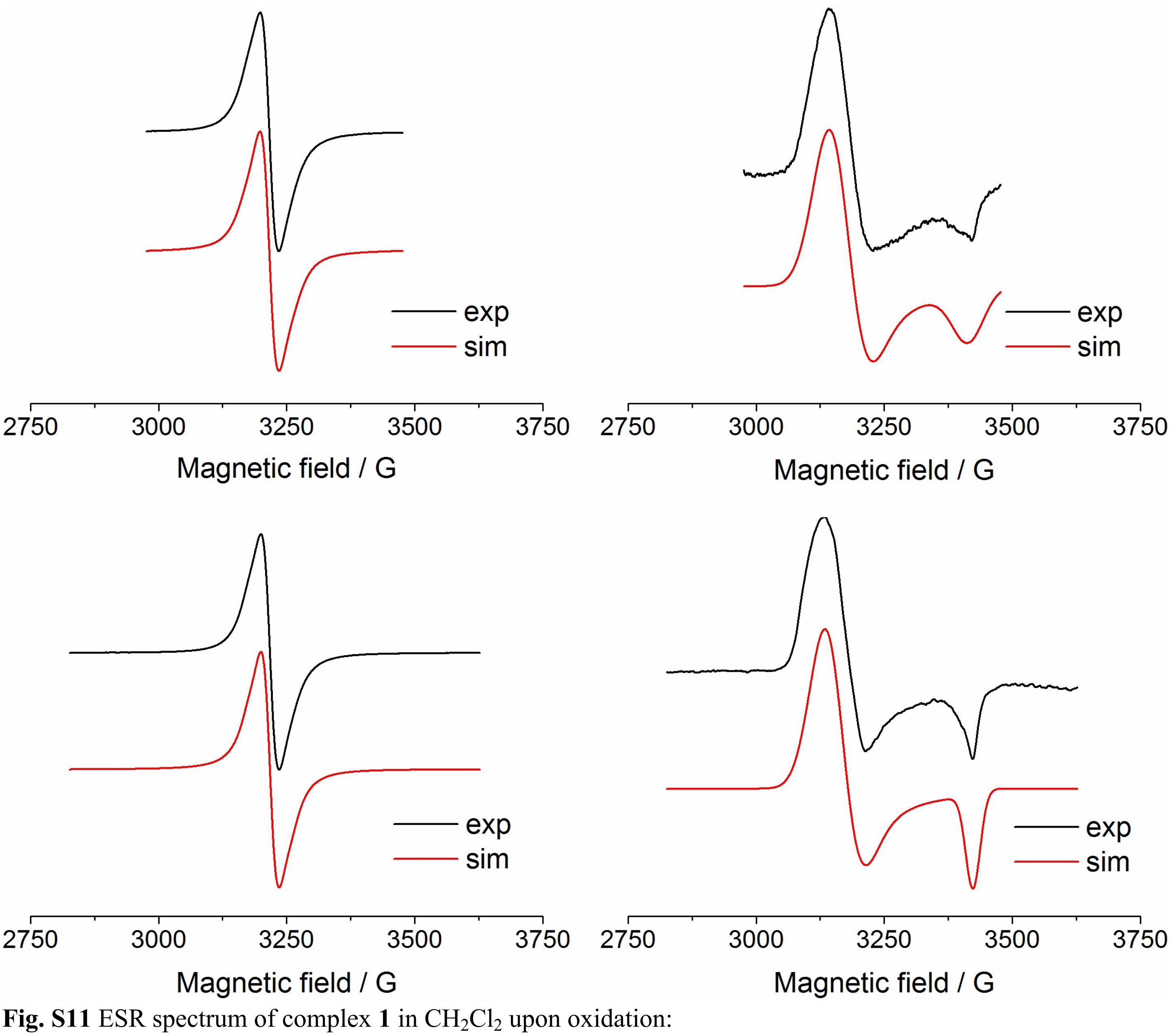

Fig. S11 ESR spectrum of complex **1** in CH_2Cl_2 upon oxidation:
left center – 295 K, 0.005 M: $g = 2.148$, $\Delta H = 30$ G, $a_{105Pd} = 15$ G, $\Delta H = 27$ G; right center – 135 K, 0.05 M: $g_{\perp} = 2.19$, $\Delta H = 75$ G; $g_{\parallel} = 2.03$, $\Delta H = 60$ G;
left bottom – 295 K, 0.1 M: $g = 2.148$, $\Delta H = 29$ G, $a_{105Pd} = 15$ G, $\Delta H = 24$ G; right bottom – 135 K, 0.1 M: $g_{\perp} = 2.19$, $\Delta H = 70$ G; $g_{\parallel} = 2.02$, $\Delta H = 28$ G.

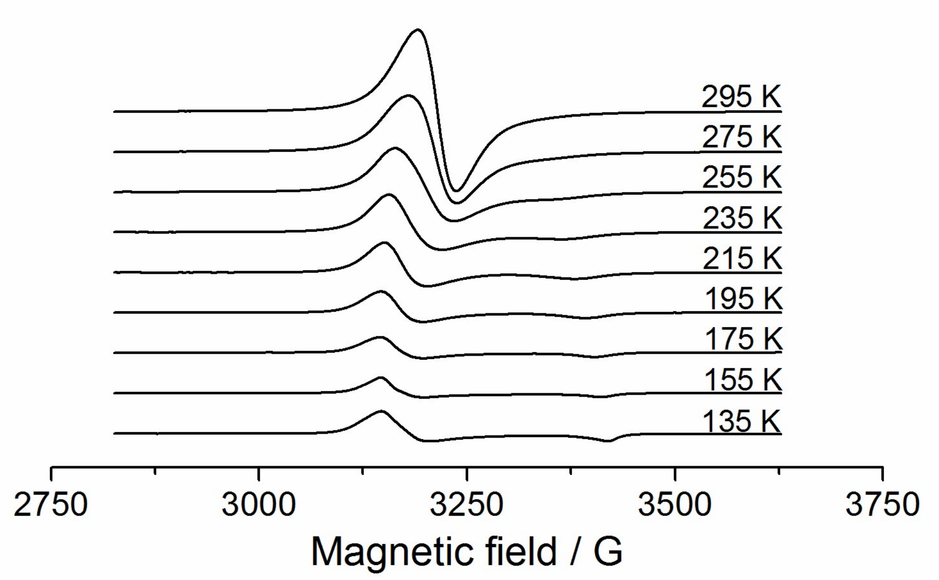

Fig. S12 Temperature dependence of complex **2** ESR spectrum in CH_2Cl_2 upon oxidation (0.1 M).

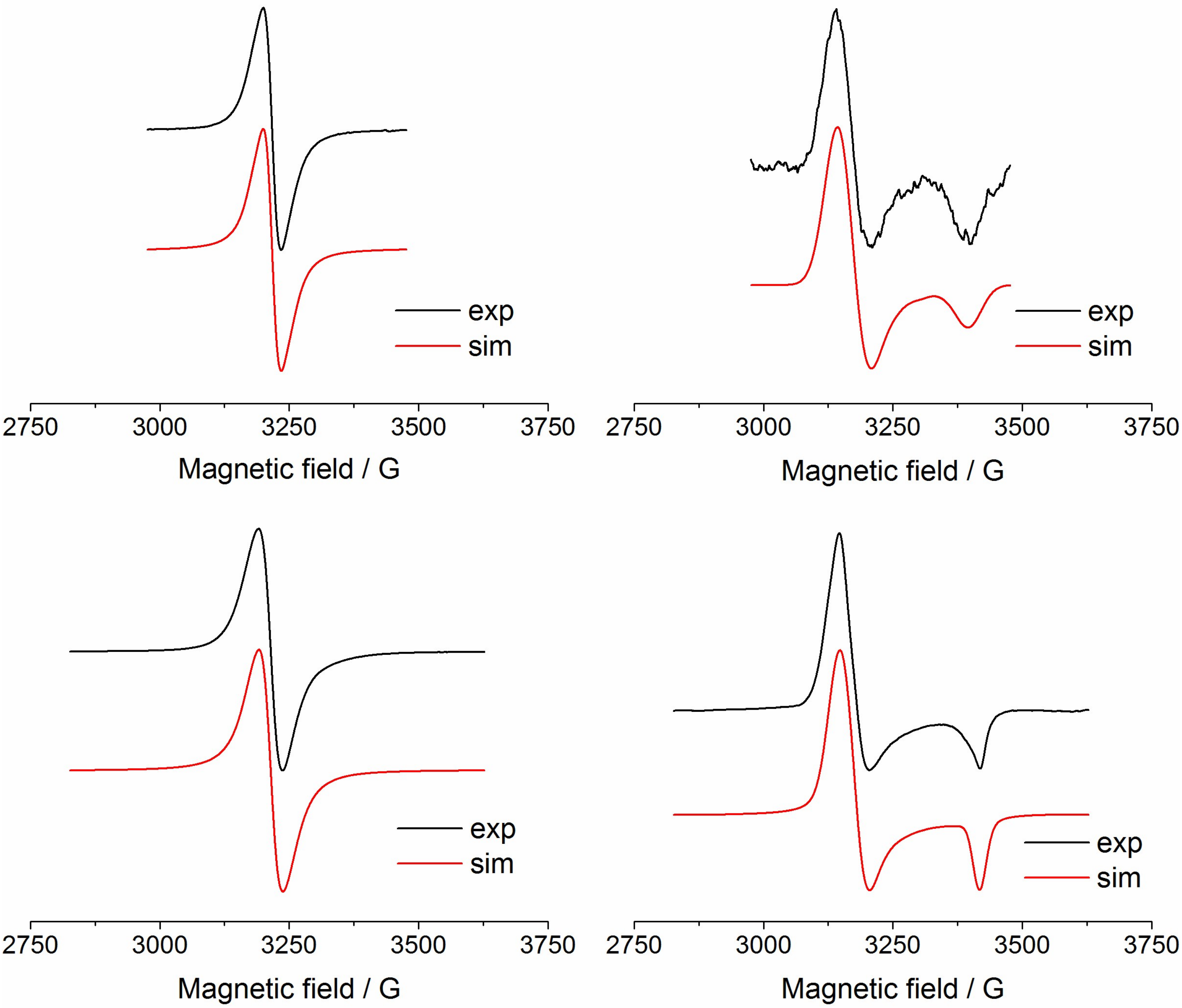

Fig. S13 ESR spectrum of complex **2** in CH_2Cl_2 upon oxidation:
left top – 295 K, 0.005 M: $g = 2.147$, $\Delta H = 28$ G, $a_{105Pd} = 13$ G, $\Delta H = 24$ G; right top – 175 K, 0.005 M: $g_{\vdash} = 2.19$, $\Delta H = 59$ G; $g_{\|} = 2.04$, $\Delta H = 50$ G;
left bottom – 295 K, 0.1 M: $g = 2.147$, $\Delta H = 37$ G, $a_{105Pd} = 13$ G, $\Delta H = 32$ G; right bottom – 135 K, 0.1 M: $g_1 = 2.20$, $\Delta H = 40$ G; $g_2 = 2.18$, $\Delta H = 40$ G; $g_3 = 2.02$, $\Delta H = 25$ G.

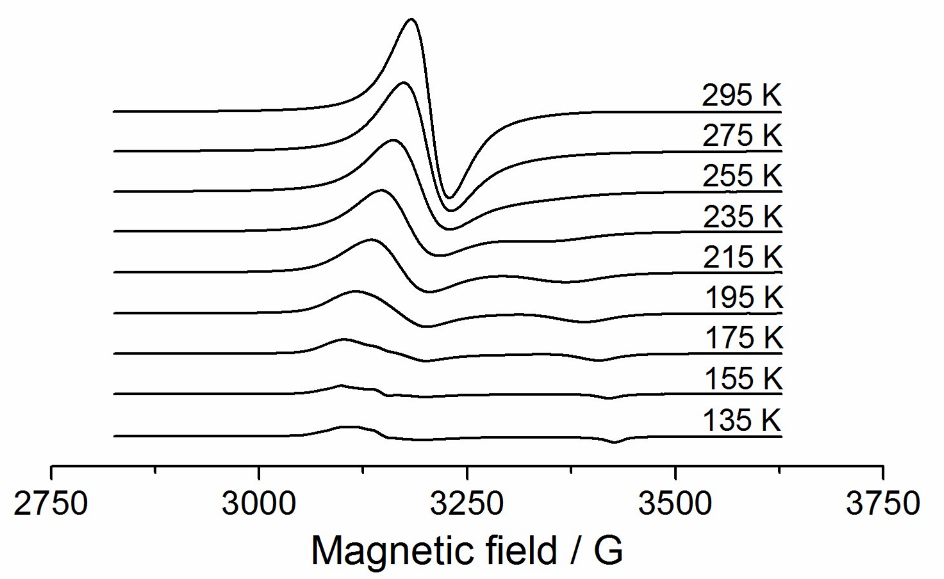

Fig. S14 Temperature dependence of complex **3** ESR spectrum in CH_2Cl_2 upon oxidation (0.1 M).

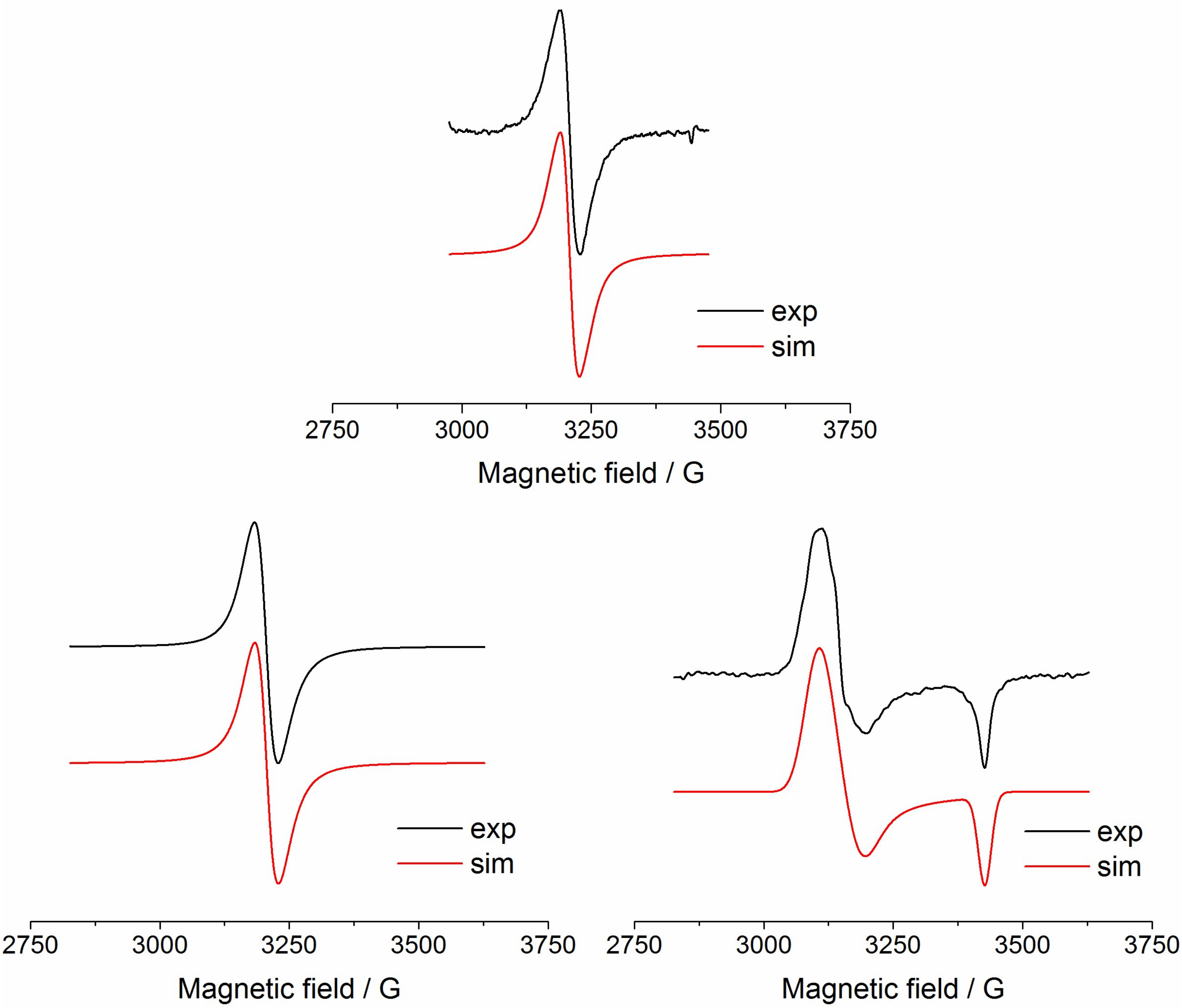

Fig. S15 ESR spectrum of complex **3** in CH_2Cl_2 upon oxidation:
top – 295 K, 0.005 M: g = 2.152, ΔH = 30 G, a_{105Pd} = 12 G, ΔH = 27 G;
left bottom – 295 K, 0.1 M: g = 2.152, ΔH = 36 G; a_{105Pd} = 12 G, ΔH = 31 G; right bottom – 135 K, 0.1 M: g_1 = 2.20, ΔH = 50 G; g_2 = 2.18, ΔH = 60 G; g_3 = 2.02, ΔH = 25 G.

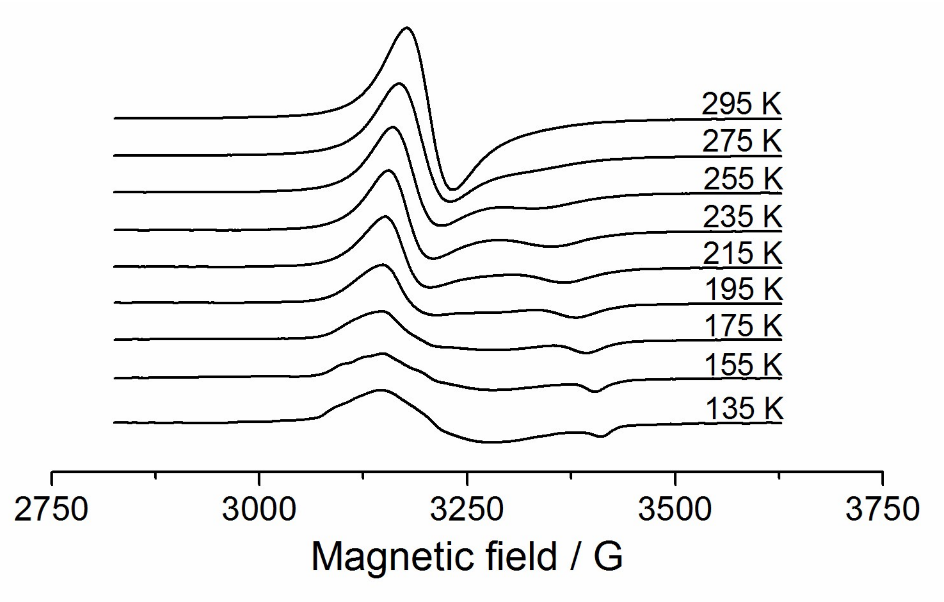

Fig. S16 Temperature dependence of complex **4** ESR spectrum in CH_2Cl_2 upon oxidation (0.1 M).

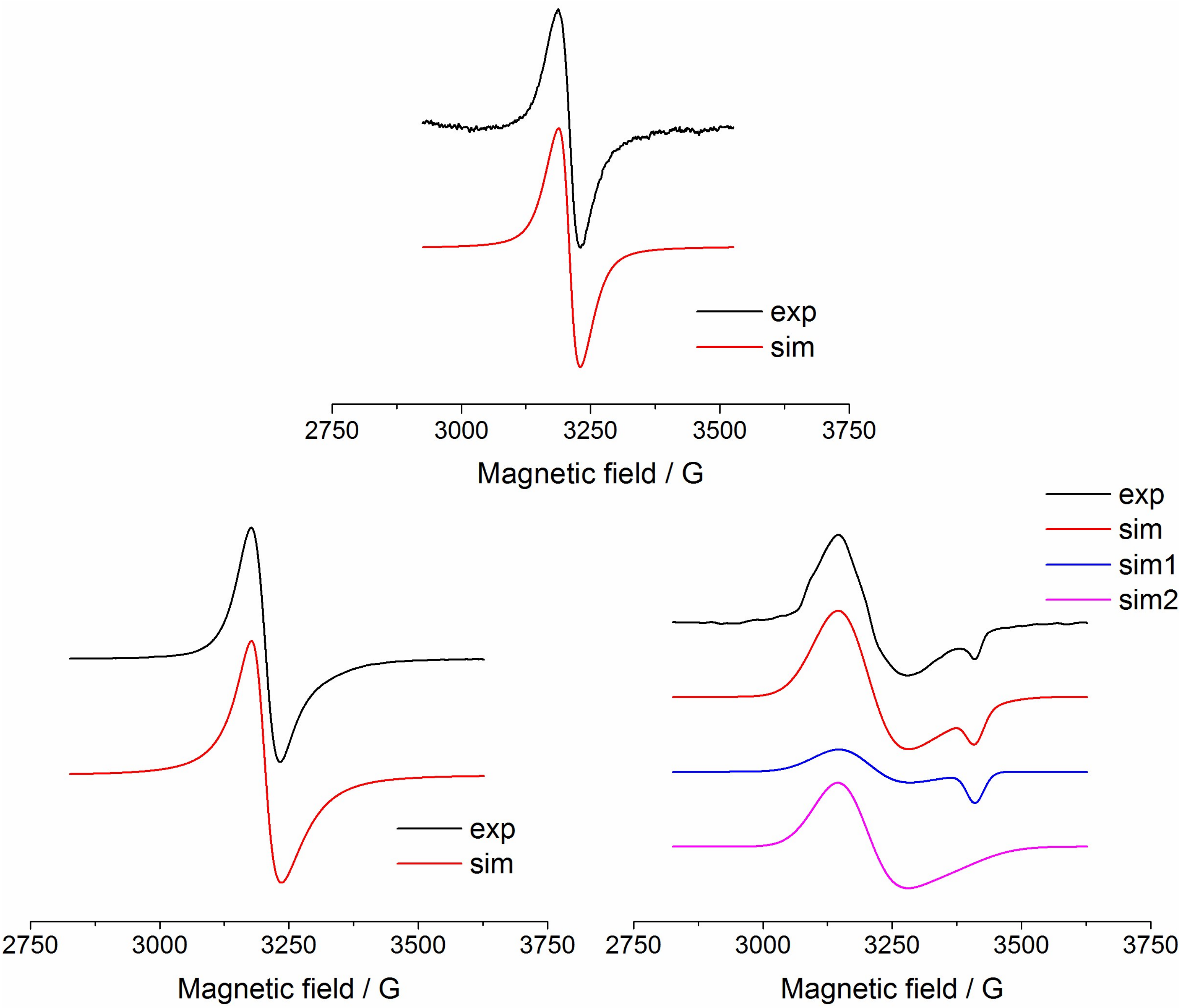

Fig. S17 ESR spectrum of complex **4** in CH_2Cl_2 upon oxidation:
top – 295 K, 0.005 M: g = 2.153, ΔH = 34 G, a_{105Pd} = 12 G, ΔH = 30 G;
left bottom – 295 K, 0.1 M: $g_{\perp}$ = 2.16, ΔH = 45 G; $g_{\|}$ = 2.13, ΔH = 100 G; right bottom – 135 K, 0.1 M: sim1: $g_{\perp}$ cannot be determined; $g_{\|}$ = 2.03, ΔH = 30 G; sim2: $g_{\perp}$ = 2.17, ΔH = 110 G; $g_{\|}$ = 2.06, ΔH = 150 G.

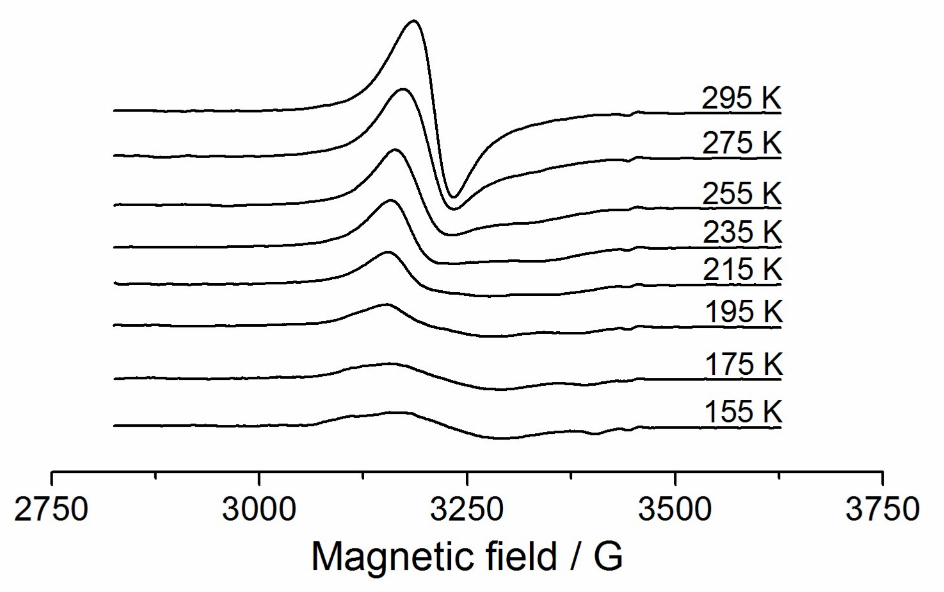

Fig. S18 Temperature dependence of complex **5** ESR spectrum in CH_2Cl_2 upon oxidation (0.1 M).

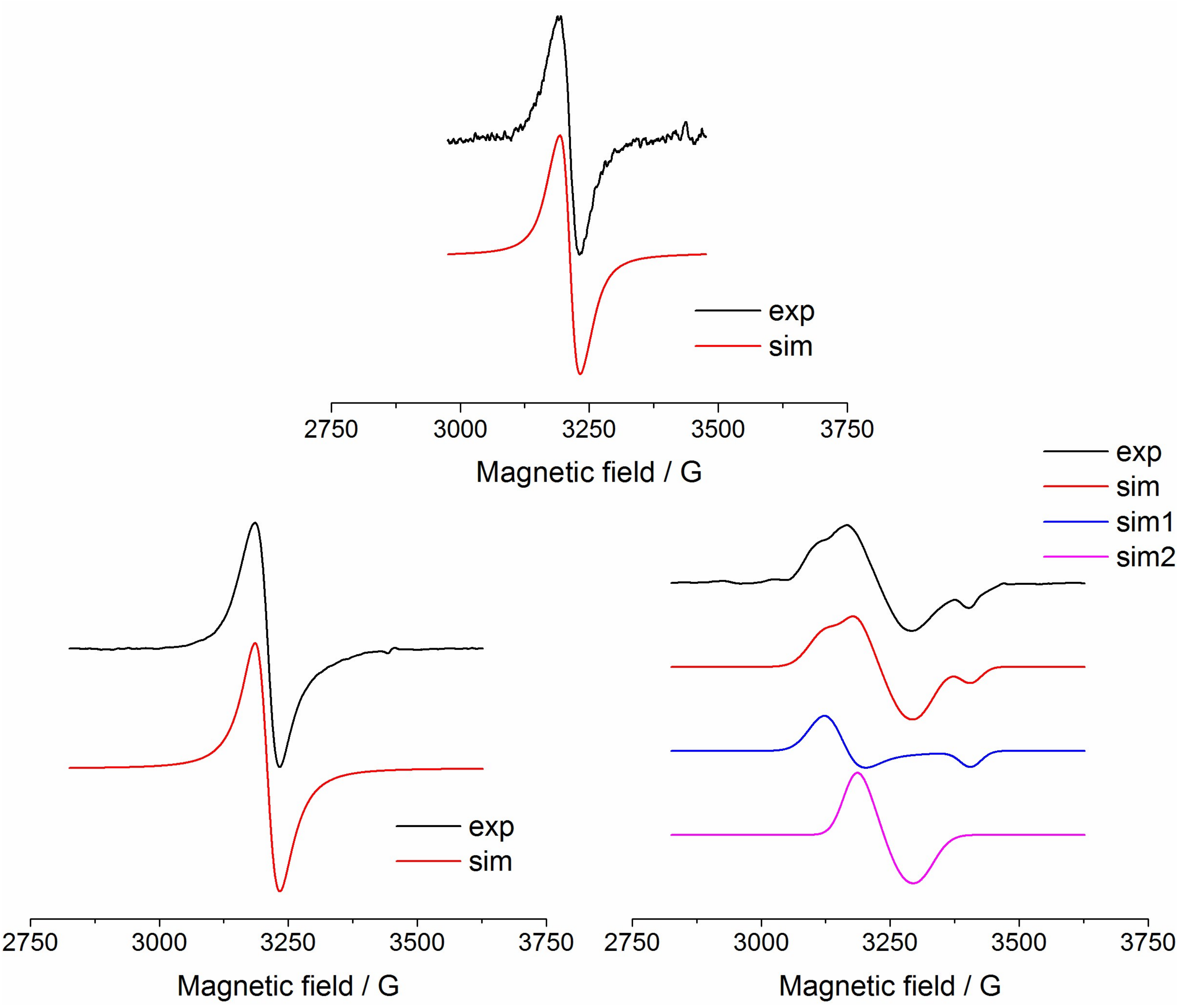

Fig. S19 ESR spectrum of complex **5** in CH_2Cl_2 upon oxidation:
top – 295 K, 0.005 M: g = 2.150, ΔH = 31 G, a_{105Pd} = 12 G, ΔH = 26 G;
left bottom – 295 K, 0.1 M: $g_{\vdash}$ = 2.16, ΔH = 45 G; $g_{\parallel}$ = 2.13, ΔH = 100 G; right bottom – 155 K, 0.1 M: sim1: $g_{\vdash}$ = 2.20, ΔH = 70 G; $g_{\parallel}$ = 2.03, ΔH = 40 G; sim2: g_1 = 2.17, ΔH = 50 G; g_2 = 2.13, ΔH = 60 G; g_3 = 2.09, ΔH = 60 G.

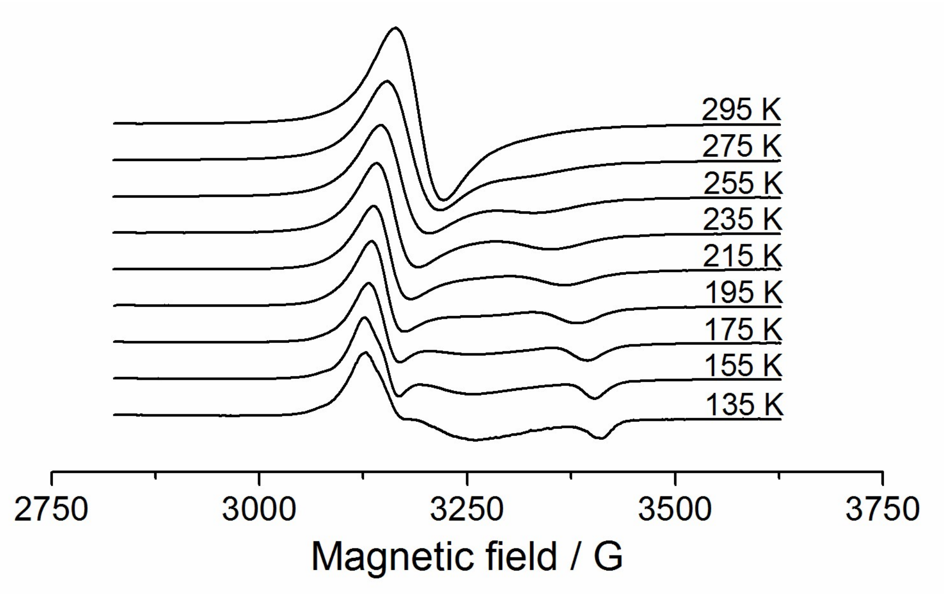

Fig. S20 Temperature dependence of complex **6** ESR spectrum in CH_2Cl_2 upon oxidation (0.1 M).

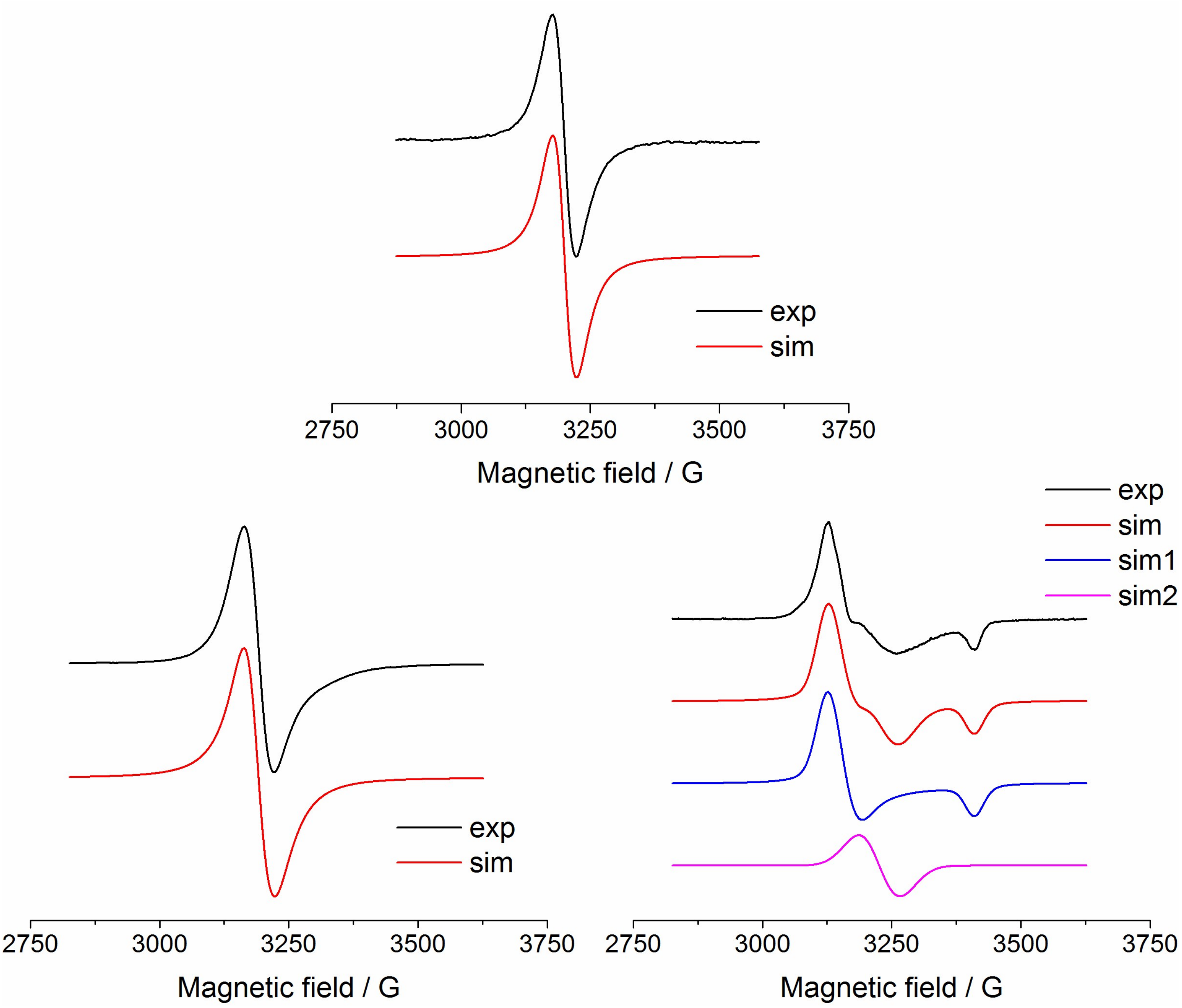

Fig. S21 ESR spectrum of complex **6** in CH_2Cl_2 upon oxidation:
top – 295 K, 0.005 M: g = 2.159, ΔH = 36 G, a_{105Pd} = 10 G, ΔH = 31 G;
left bottom – 295 K, 0.1 M: $g_{\perp}$ = 2.17, ΔH = 50 G; $g_{\parallel}$ = 2.15, ΔH = 60 G; right bottom – 135 K, 0.1 M: sim1: g_1 = 2.21, ΔH = 40 G; g_2 = 2.19, ΔH = 50 G; g_3 = 2.03, ΔH = 35 G; sim2: g = 2.14, ΔH = 40 G.

Quantum chemical calculations details

Using complex **3** as an example we investigated the influence of geometry parameters on the result of energy characteristics estimation: geometry parameters were optimized at the B3LYP/TZP-DKH level. In this case HOMO is appear to be stabilized by 0.365 eV while LUMO energy increases by 0.205 eV. This leads to noticeable increase in the energy gap value by 0.239 eV compared to one obtained with X-ray geometry. In [1,2] example compounds consisting of the 1st and 2nd rows elements (database IP131 [3]) illustrate the long-range corrected functionals describe the frontier orbitals energy and the energy gap value better than B3LYP. Hereat we examined the influence of the functional on the energy characteristics. In the case of cyclopalladated complexes no enhancement of E_{HOMO} and $\Delta E_{(\mathrm{HOMO\text{-}LUMO})}$ values were obtained: CAM-B3LYP-based calculations afford significant stabilization of HOMO (by ~ 1.5 eV regardless to the geometry used) and severe increase of LUMO energy resulted in increase of $\Delta E_{(\mathrm{HOMO\text{-}LUMO})}$ by ~ 2.7 eV in comparison to values obtained at B3LYP level. Using the ωB97X-D functional makes these shifts even more noticeable: stabilization of LUMO achieves ~ 2.1 eV and $\Delta E_{(\mathrm{HOMO\text{-}LUMO})}$ increases by 3.3-3.8 eV. Thuswise, in the present work we discuss the results obtained at B3LYP/TZP-DKH level.

Table S1 Calculated energies (in eV) of frontier orbitals and energy gap for complex **3** in CH_3CN

	B3LYP		**CAM-B3LYP**		**ωB97X-D**	
	X-Ray geo	**Opt B3LYP**	**X-Ray geo**	**Opt B3LYP**	**X-Ray geo**	**Opt B3LYP**
HOMO	-5.390	-5.755	-6.937	-7.322	-7.459	-7.85
LUMO	-1.52	-1.495	-0.354	-0.316	0.258	-0.282
ΔE	3.87	4.26	6.583	7.006	7.717	7.568

[1] Jorge, F. E.; Canal Neto, A.; Camilett, G. G.; Machado, S. F. *J. Chem. Phys.* **2009**, *130*, 064108-1–064108-6.

[2] Tomasi, J.; Mennucci, B.; Cammi, R. *Chem. Rev.* **2005**, *105*, 2999-3093.

[3] Ramsay, W.; Foster, R. *Nature* **1949**, *163*, 178–179.

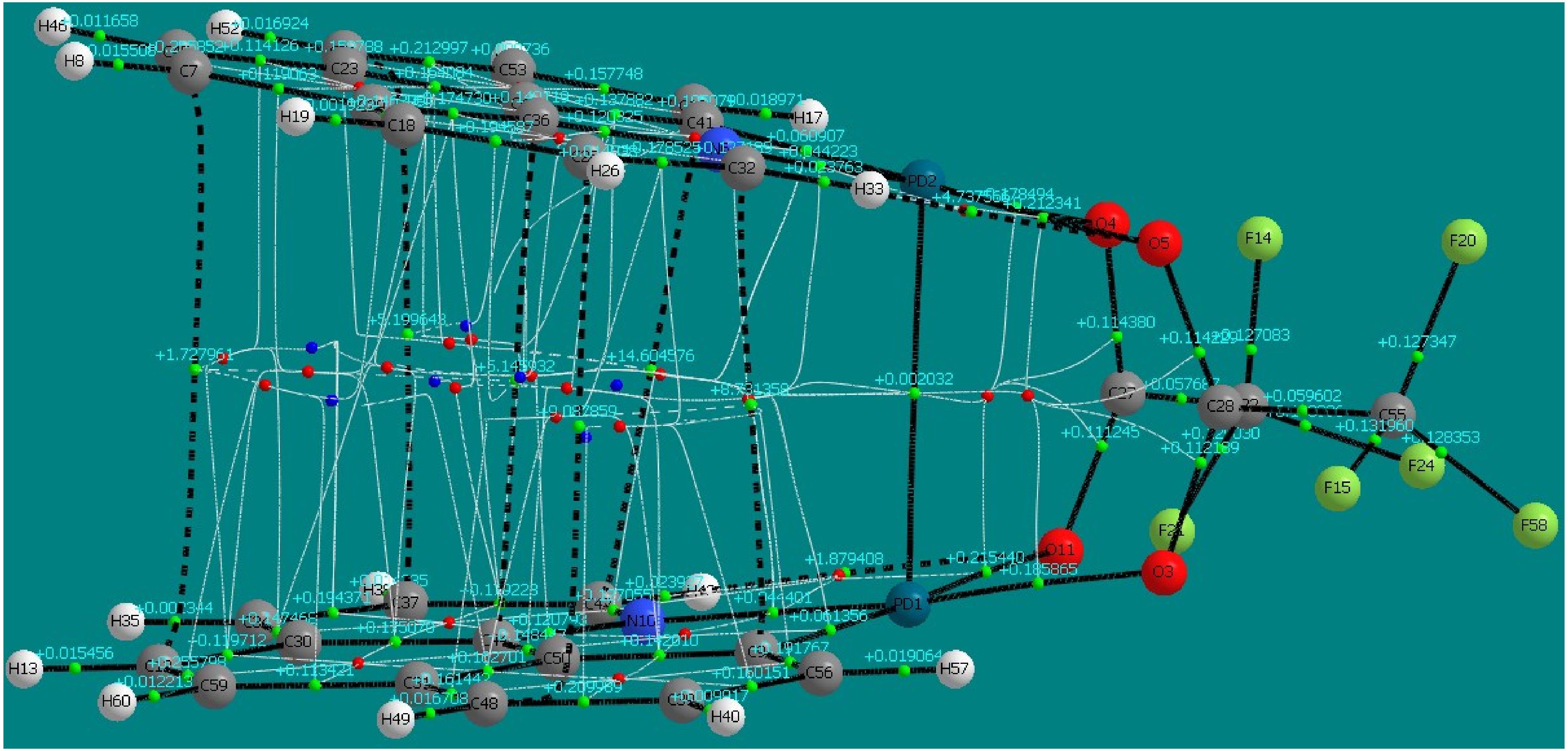

Fig. S22 Complex **4** in CH_2Cl_2.

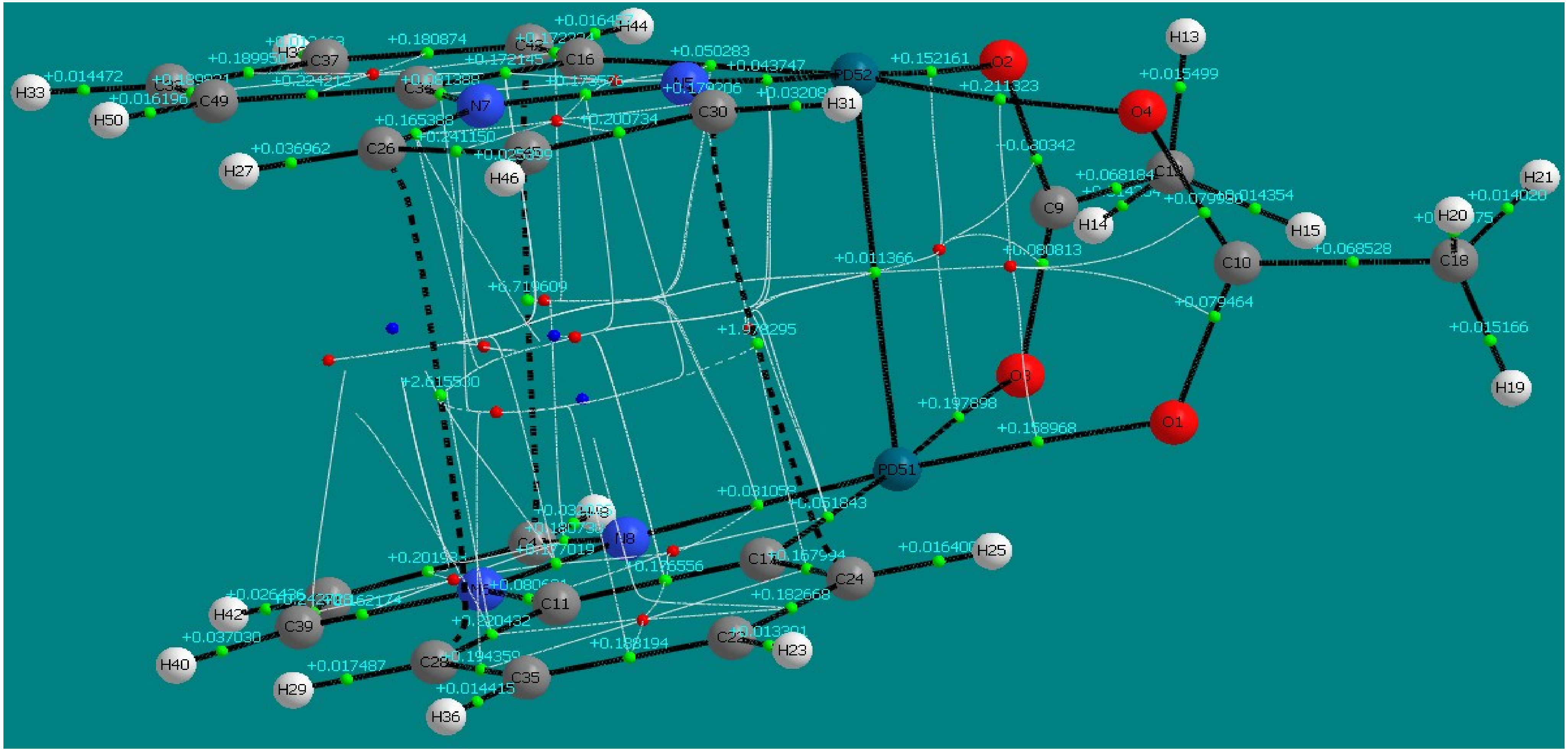

Fig. S23 Complex **3** in CH_2Cl_2.

NMR spectra

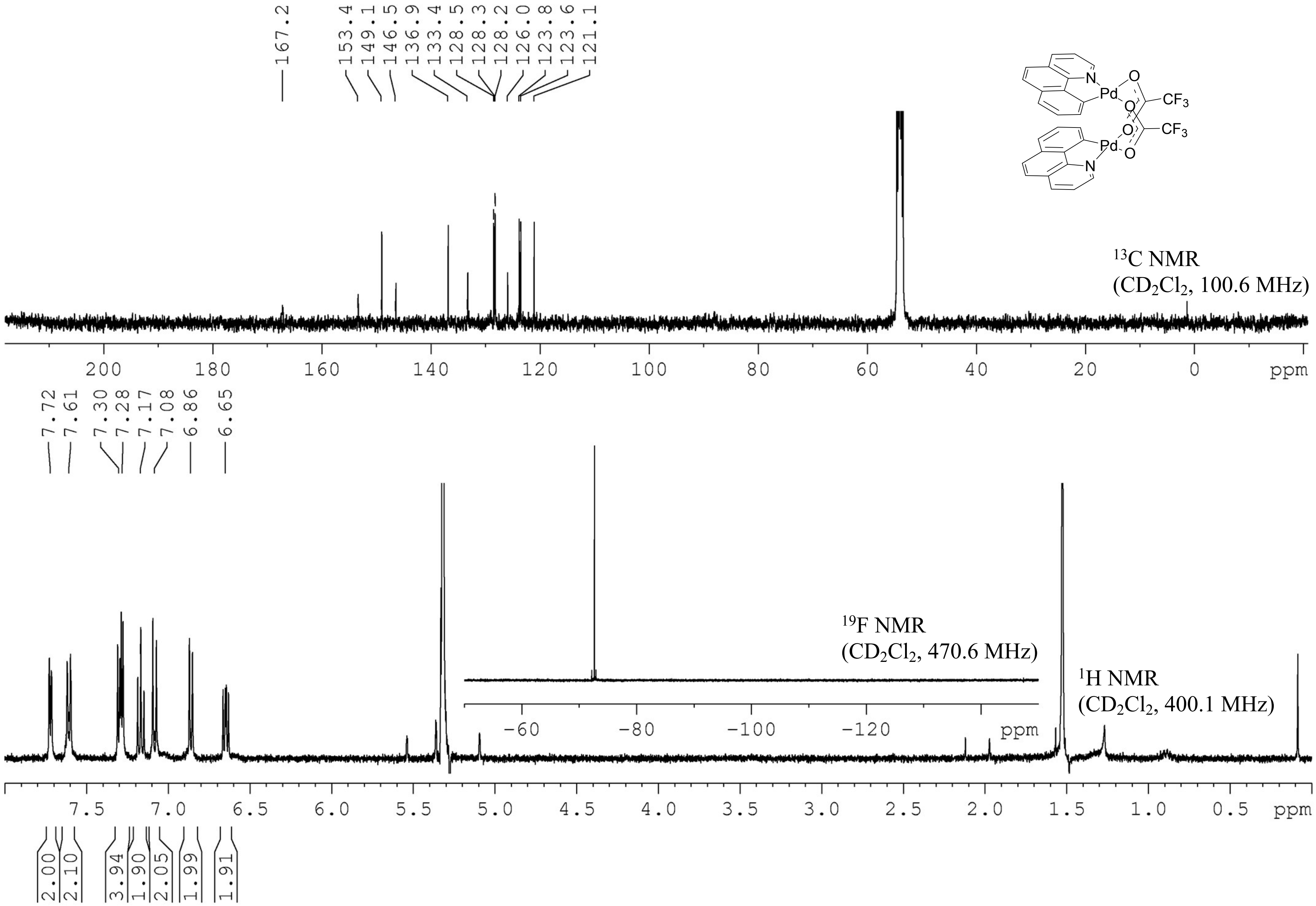

Fig. S24 NMR spectra of complex **5** [(bhq)Pd(OCOCF$_3$)]$_2$.

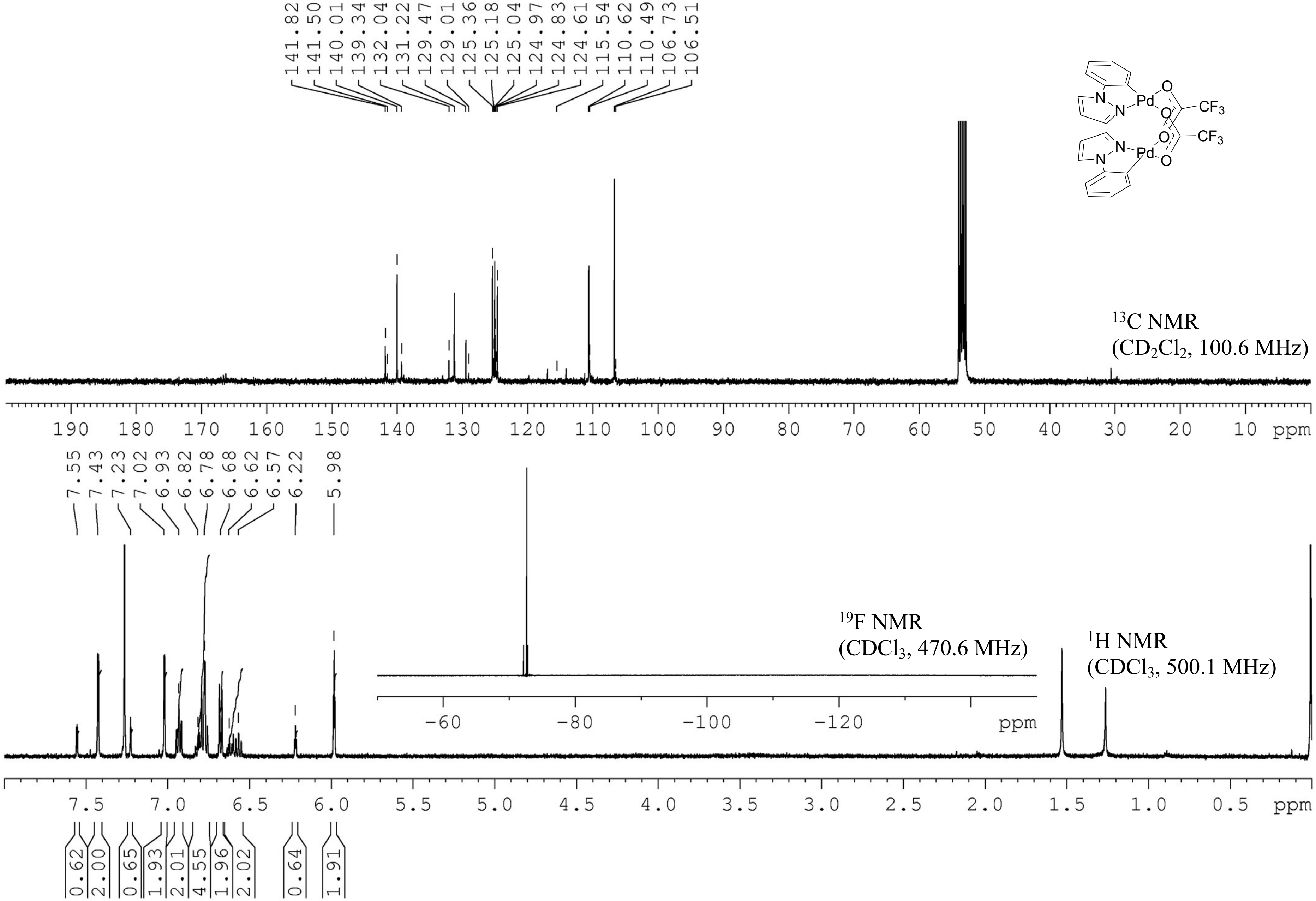

Fig. S25 NMR spectra of complex **6** [(phpz)Pd(OCOCF$_3$)]$_2$.

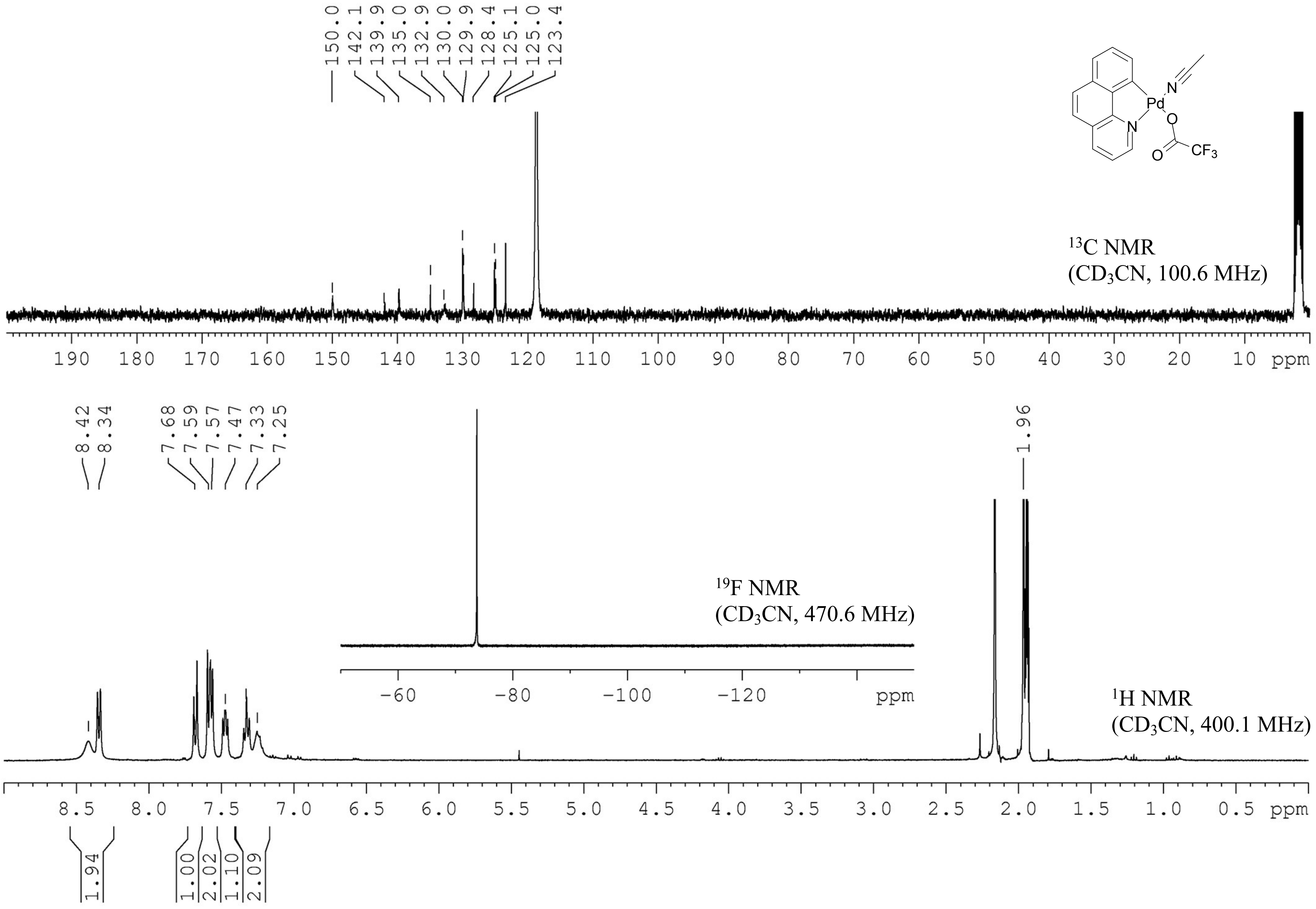

Fig. S26 NMR spectra of complex **11** (bhq)Pd(OCOCF$_3$)(CH$_3$CN).

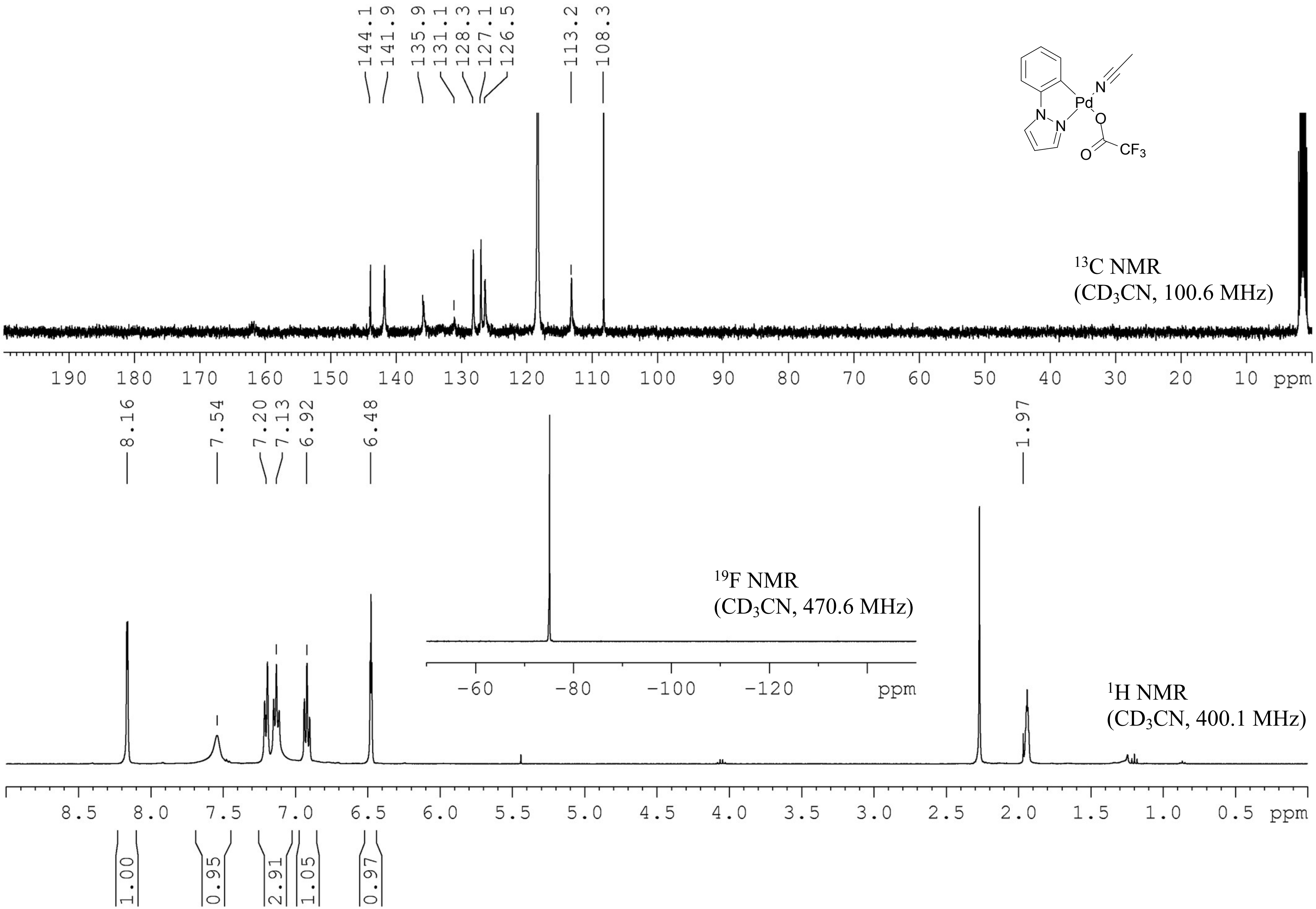

Fig. S27 NMR spectra of complex **12** (phpz)Pd(OCOCF$_3$)(CH$_3$CN).

Mass spectra

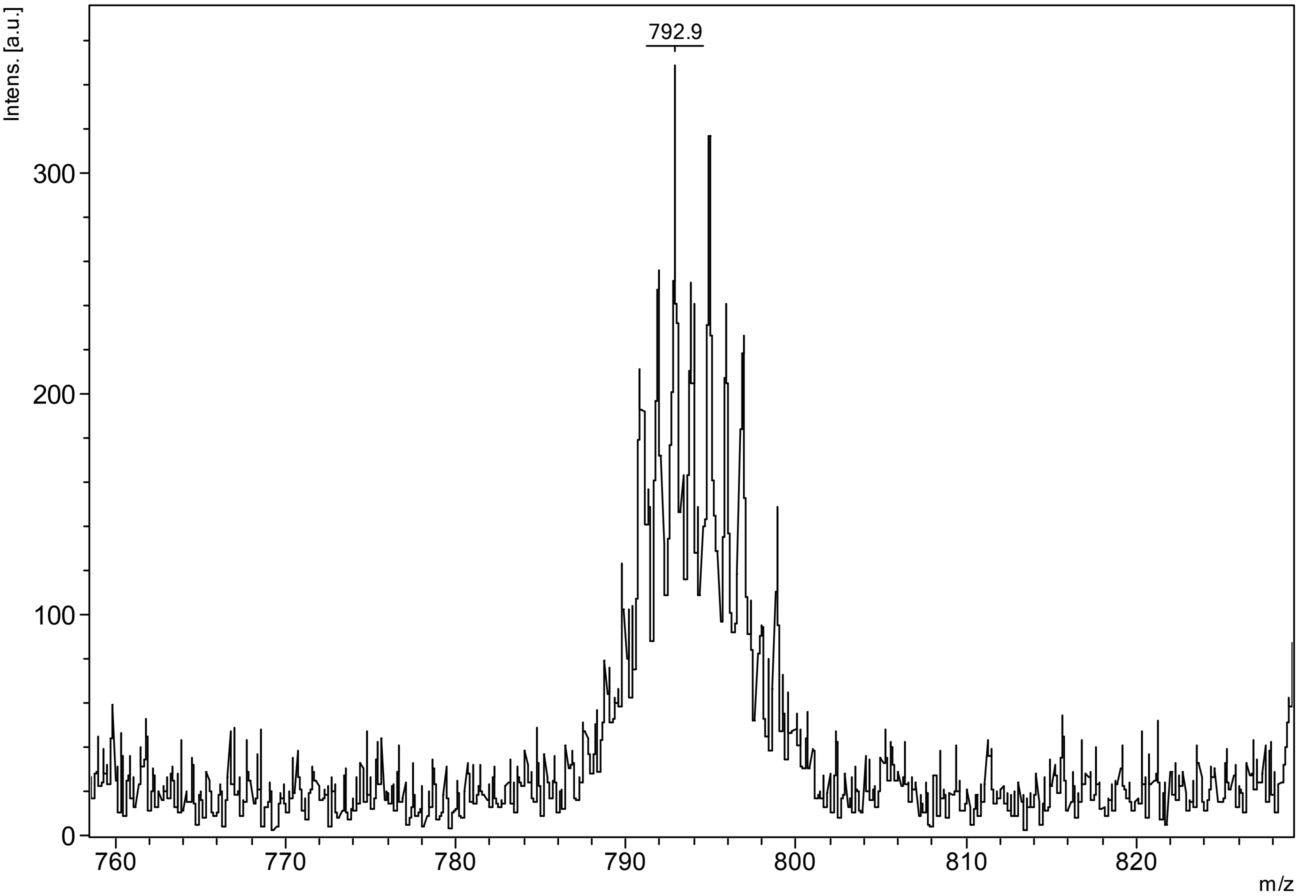

Fig. S28 MALDI-MS of complex **5** $[(bhq)Pd(OCOCF_3)]_2$.

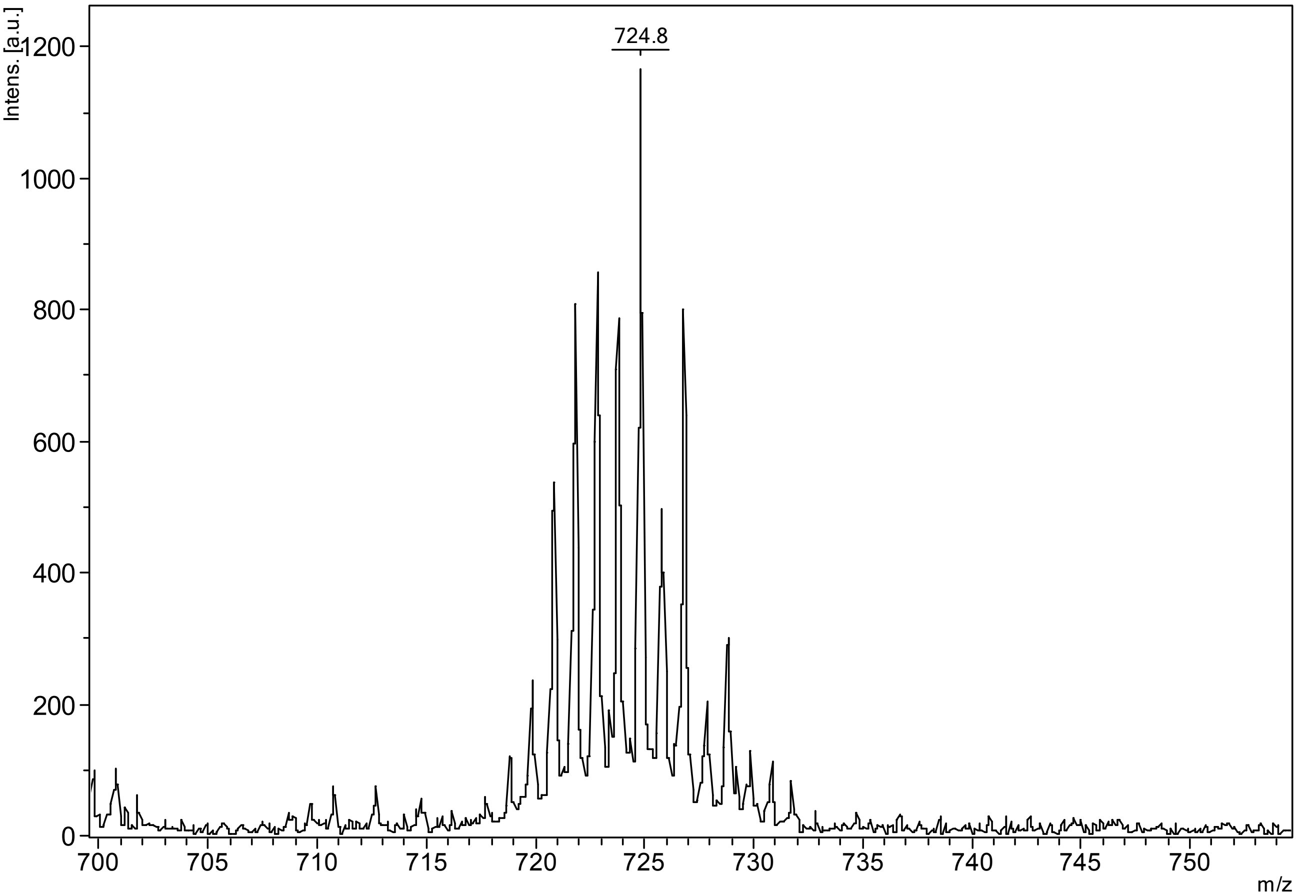

Fig. S29 MALDI-MS of complex **6** $[(phpz)Pd(OCOCF_3)]_2$.

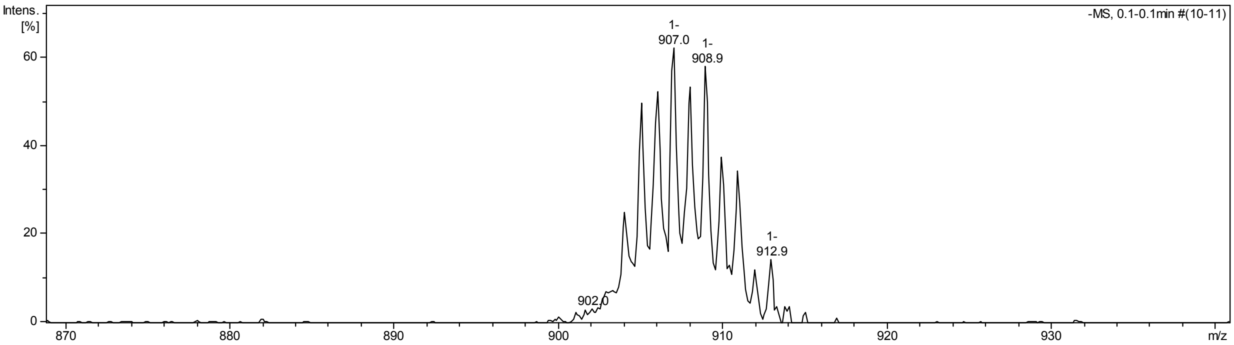

Fig. S30 ESI-MS of complex **5** [(bhq)Pd(OCOCF$_3$)]$_2$.

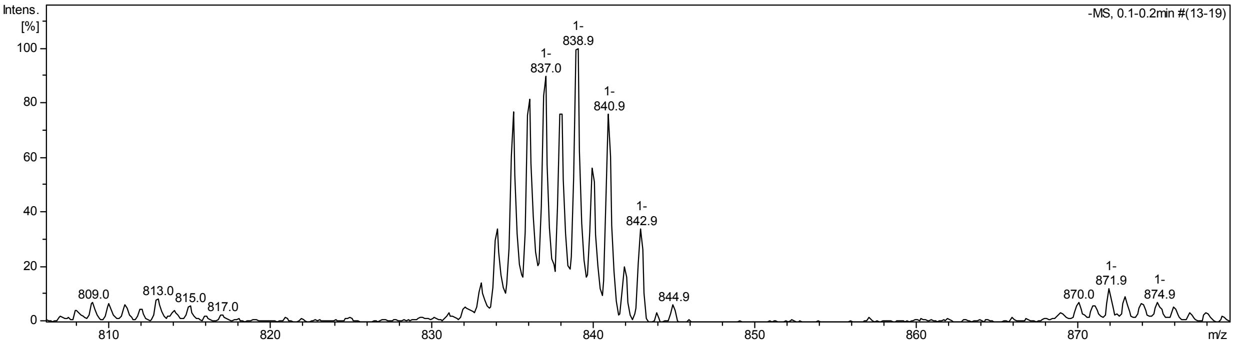

Fig. S31 ESI-MS of complex **6** [(phpz)Pd(OCOCF$_3$)]$_2$.

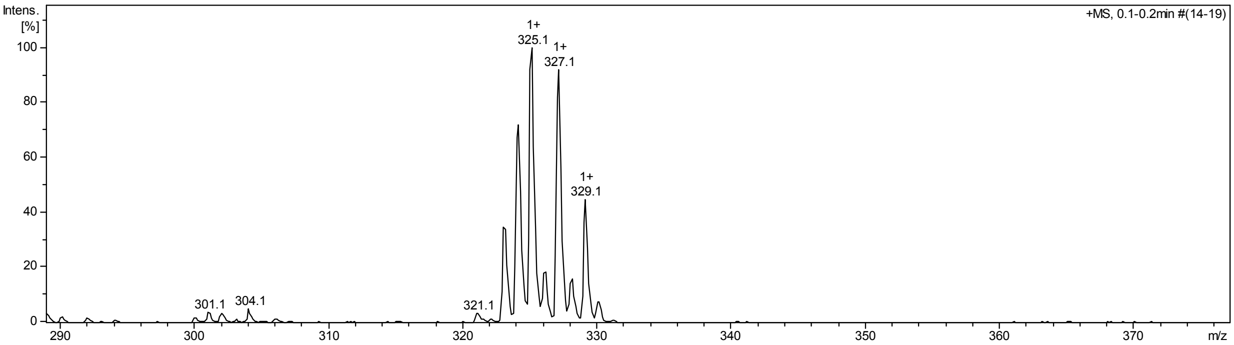

Fig. S32 ESI-MS of complex **11** (bhq)Pd(OCOCF$_3$)(CH$_3$CN).

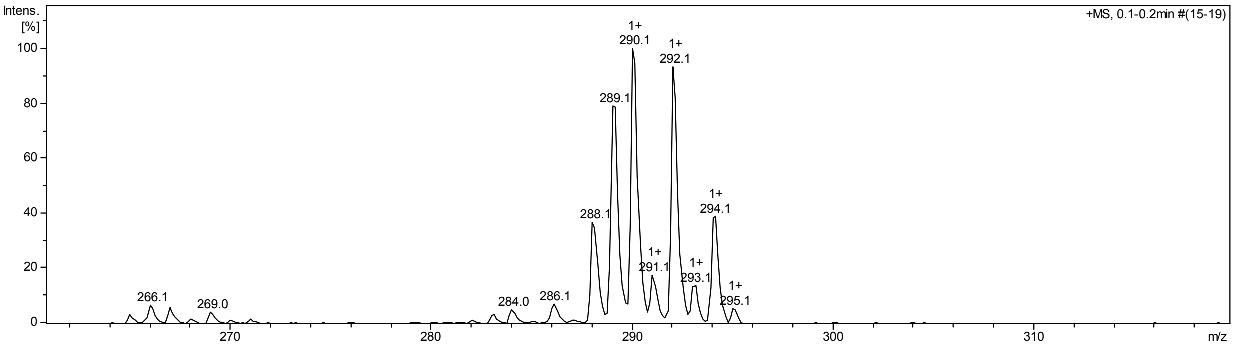

Fig. S33 ESI-MS of complex **12** (phpz)Pd(OCOCF$_3$)(CH$_3$CN).